Hindawi
Shock and Vibration
Volume 2019, Article ID 6405809, 20 pages
https://doi.org/10.1155/2019/6405809

Research Article

Adaptability of Turbulence Models for Pantograph Aerodynamic Noise Simulation

Xiao-ming Tan, Peng-peng Xie, Zhi-gang Yang, and Jian-yong Gao

Key Laboratory of Traffic Safety on Track (Central South University), Ministry of Education, School of Traffic and Transportation Engineering, Central South University, Changsha 410075, Hunan, China

Correspondence should be addressed to Zhi-gang Yang; sound_wdq@csu.edu.cn

Received 20 December 2018; Accepted 21 February 2019; Published 12 March 2019

Academic Editor: Franck Poisson

This study was targeted at CX-PG-type Faiveley pantograph of high-speed train and cylinders and analysed the fluctuating flow field around these objects by using the large eddy simulation (LES) model, the scale adaptive simulation (SAS) model, the improved delayed detached eddy simulation with shear-stress transport-kω (IDDES sst-kω) model, the delayed detached eddy simulation with shear-stress transport-kω (DDES sst-kω) model, and the delayed detached eddy simulation with realizable-kε (DDES R-kε) model. The space distributions of velocity, vorticity, and vortex structures were compared to investigate their performances on simulating fluctuating flow fields and computing aeroacoustic sources through Fourier transformation based on the surface fluctuating pressures. Furthermore, the far-field radiated noise was calculated based on the Ffowcs Williams–Hawkings equation. Based on the computation precision of the five models, a feasible turbulent model was selected for simulating aerodynamic noise. The relative errors to the results from wind-tunnel experiments of the sound pressure level (SPL) were obtained as 0.7%, 1.6%, 7.8%, 3.8%, and 12.1%, respectively, and the peak Strouhal numbers were obtained as 2.0%, 8.5%, 5.5%, 11.5%, and 51.0% for cylinder simulation. Moreover, the relative errors of SAS, IDDES sst-kω, DDES sst-kω, and DDES R-kε models to the result from LES of SPL were respectively obtained as 2.3%, 4.5%, 5.6%, and 10.8% for pantograph. Thus, it is conclusive that none of the aforementioned models are comparable with the LES model with respect to the precision in the aeroacoustic simulation. However, SAS, IDDES sst-kω, and DDES sst-kω are practically competent with the LES model considering the numerical simulations with respect to the engineering computation precision. The numerical computation model was verified using the wind-tunnel test results.

1. Introduction

Aerodynamic noise of high-speed train is an outstanding factor that restricts China's stepping outside into world with the increase of operation speed [1, 2]. A smooth design can control the aerodynamic noise level of train body to a large extent; this inversely increases the contribution ratio of noise of unsmoothed components, such as pantograph and bogies, making them the main noise sources. The test results obtained from a real-train running at 330 km/h indicate that the contribution rates of radiation noise from pantograph accounts to more than 10% of the total noise. Researchers mainly investigated sound-generation mechanism and aeroacoustic optimization of pantograph through experiments [3–8] and numerical simulations [9–23]. Such a numerical simulation has attracted a considerable amount of attention because of its advantages of short term, low cost, and the use of multiple flow-acoustic information, compensating for wind-tunnel and real-train tests.

A pantograph is composed of a series of bars with different dimensions and angles. The Reynolds number of these bars lies within the interval of $[1 \times 10^5, 2 \times 10^6]$, which belongs in the range of high subcritical Reynolds numbers and resistance crisis zone when the inflow velocity is 350 km/h. The cylinder flow field in this interval covers complicated phenomena, such as the separation of boundary layer of laminar-turbulent flow, vortex streets, flow transition, and large separation turbulence. The flow field of a pantograph may exhibit these phenomena as well as mutual interferences. The accurate simulation of the fluctuating flow field of these

flow-field phenomena is critical for accurately predicting the full-range of the aerodynamic noise spectrum of the pantograph. This poses a huge challenge to the turbulence models.

The LES model is a mainstream turbulence model for simulating the fluctuating flow field around the pantograph and has achieved good simulation results. Studies [9–12] have utilized LES to simulate the fluctuating flow field around the pantograph and calculated the spatial distribution of the dipole noise source according to the vortex sound theory. The corresponding simulation results of fluid-acoustic field have shown good consistency with experimental data. In addition, the studies revealed that a proper panhead pillar can destroy the shedding vortex street structure, thus effectively depressing the aerodynamic noise radiated from the panhead [9–12]. Sun and Xiao [13] and Zhang et al. [14] studied the fluid-acoustic field characteristics of a pantograph by using an LES model, an acoustic boundary element method, and a Ffowcs Williams–Hawkings (FW-H) equation and concluded that high-frequency noise mainly originates from panheads [13] and the noise radiated from open-type pantographs is 3.4 dBA lesser than that from closed-type pantographs [14]. Rho et al. [15] employed the LES model, FW-H equation, and a genetic-algorithm-based kriging model to create an aeroacoustic optimization design for the intersection shape of a panhead. Moreover, they conducted wind-tunnel tests to validate the accuracy of the optimization results. The optimized shape was assembled on a pantograph and achieved 26% and 2 dB decrease in resistance and noise levels, respectively. Holmes et al. [16] focused on the sound-generation mechanism of outer-convex cavity-type fairwater sleeve by using an LES model and acoustic boundary element method. They determined that the lateral eddy shedding from the guide edges of a cavity impact the trailing edges, forming intensive fluctuating pressure inside the cavity and radiating noise outside. Moreover, they proposed that shape optimization of fairwater sleeve is conducive for depressing the radiation noise from the cavity. Lee et al. [17] discussed the contributions of components of a closed-type pantograph to the aeroacoustic spectrum under 400 km/h by means of an LES model and the FW-H equation; they revealed that noise within the frequency bands of 60–400, 600–800, 1000–2000, and 2000–5000 Hz was mainly derived from the bottom frame area, panhead area, knuckle area between the upper and lower arms, and whole pantograph, respectively.

Furthermore, models, such as the DDES, IDDES, and SAS have also caught attentions of researchers. Liu et al. [18] investigated the characteristics of the fluid-acoustic field of cylindrical bars under varied angles of attack and inflow velocities by using the DDES model and FW-H equation; they indicated a larger angle of attack corresponds with a lower-peak sound pressure level (SPL) and frequency. Zhang et al. [19] applied the DDES model and FW-H equation to analyse the effects of connection and disconnection between an air conditioner set and a pantograph fairwater sleeve on the radiated noise. They concluded that the aeroacoustic performance is superior under the disconnection condition between. Kim [20] simplified the pantograph and a settlement platform into a cylinder and concave cavity, respectively, and then probed the influence of the assembling positions and fillets of guide edges on aeroacoustics. The results showed that the length of the recirculation zone, upstream of the cavity, and the strength of the vortex reduce significantly along with the total noise radiated from the cavity and cylinder, resistance, and lateral force when the fillet angle ascends from zero to a certain angle. Additionally, decreasing the interactive interference behaviours of shear flow and cylinder is effective with the increase in the distance between guide edge and cylinder; this in turn undermines the peak SPL. Lei et al. [21] implemented the SAS model and acoustic boundary element method to compute aeroacoustics of a closed-type pantograph under 300 km/h and determined eddy shedding as the main factor contributing to the formation mechanism of aerodynamic noise. Further, Siano et al. [22] calculated far-distance noise of a pantograph through a URANS model and an FW-H equation. However, the frequency spectrum curve obtained from a simulation does not agree with the experimental curve near the peak frequency zone.

It is worth noting that in the aforementioned literature, the simulation results of the URANS model were not very good for determining the pantograph aerodynamic noise; however, the simulation results of the advanced turbulence model were reasonable. Unfortunately, none of the aforementioned studies examined these advanced turbulence models to simulate the performance of the fluctuating flow field, aerodynamic noise source, and radiated noise of a pantograph. This paper does not evaluate the accuracy of these turbulence models to simulate the fluctuating flow field around a pantograph but attempts to assess their adaptability for simulating the aerodynamic noise of a pantograph according to their simulation of the fluctuating flow field, aerodynamic noise source, and radiative noise. As pantographs are composed of rod structures, it is necessary to evaluate their adaptability for the aerodynamic noise simulation of cylinders. Therefore, this paper first discusses the applicability of the advanced turbulence model to the numerical simulation of cylindrical aerodynamic noise and then discusses the applicability of the advanced turbulence model to the numerical simulation of pantograph aerodynamic noise.

2. Turbulence Model

In this study, different turbulent models were employed based on an acoustic analogy method to simulate the fluctuating flow field around a pantograph. Next, the acoustic power of the sound source was formulated using the Curl far-distance integral equation, and the characteristics of aeroacoustic sound source were analysed. The far-distance radiated noise was finally predicted using the FW-H equation. Thus, the mathematical physics model includes a turbulent model part and an acoustic equation part.

LES, SAS, IDDES sst-kω, DDES sst-kω, and DDES R-kε are the turbulent models used in this study. These have been widely used and are easily available; thus, their control

equations are omitted from this paper, and their constitutive ideas, advantages, and disadvantages have been highlighted instead. For more details of the control equation of these models, please refer to [23–30]. In order to be easy to describe, LES, SAS, IDDES sst-kω, DDES sst-kω, and DDES R-kε are combined as 5 turbulence models, while SAS, IDDES sst-kω, DDES sst-kω, and DDES R-kε as the four models.

The basic idea of the LES model is to obtain the control equation of a large-eddy numerical simulation, which can describe motions of large-scale vortexes by filtering the Navier–Stokes equation by using a specific filtering method. In contrast, a sub-grid-scale stress model was applied to solve small-scale vortexes, which prevents the direct simulation of the full-scale vortex motion [23]. This model is used to equalize the airflow variables, which are solved as instantaneous values within the spatial domain, through which the pressure fluctuating phenomenon can be captured from the separated flow. Nonetheless, neither the present sub-grid-scale model is able to simulate the small-scale eddy due to the wall separation on coarse meshes nor the near-wall model to completely identify the near-wall flow structures under high Reynolds number or soundly simulate the growth and separation rules of boundary layers. Nonetheless, it matters little for its application in this research because aeroacoustic simulation of pantograph is concentrated on the phenomenon of airflow fluctuation.

The core concept of DES is to calculate small- and large-scale eddy motions by using the RANS and LES models in the near-wall-flow and turbulence-dominant domains, respectively. Moreover, a judgement function was used to transform turbulent models in different calculation domains. This methodology compensates for the demerit of the RANS model in simulating separation and helps improve the computation efficiency of the LES model with respect to boundary flow. However, the use of the DES model results in the following common problems. It is much likely to perform calculations by using LES within the boundary layer after the mesh becomes excessively dense near the wall surface; this results in lower values of Reynolds number, friction force, and eddy viscosity coefficients. This is followed by a mesh-induced separation and the nonphysical attenuation of an eddy viscosity coefficient near the wall surface [25]. DDES, proposed by Menter and Kuntz [25] and Spalart et al. [26], can solve the aforementioned problems by introducing a transition and a constraint function into the DES. The transition function can retard the influence area of RANS and relax the dependence of DES on the mesh scale, ensuring the simulation of the whole boundary layer through RANS. In addition, the constraint function can control the speed of the eddy viscosity coefficient within the normal scopes in the boundary layer. However, DDES has encountered the "Log-Layer Mismatch" problem [27] in its application, that is, in the logarithmic region of the boundary layer, the modulus of the eddy viscosity is large, so that the analytical turbulence attenuation curve is not in accordance with the actual physical properties. Shur et al. [26] integrated the merits of DDES with the LES wall-surface model and proposed IDDES, which not only effectively solved the above-mentioned problems but also accelerated the switch of RANS and LES in the separation region. Both DDES and IDDES delay the influence region of RANS, inevitably producing an exaggerated turbulence viscosity upstream. This weakens the ability of LES in capturing the turbulence structures downstream: this was termed as the grey-zone effect [29]. In addition, neither DDES nor IDDES can solve the drawback of the RANS model, that is, the solved flow-field variables are time-averaged and do not consider some details of turbulent flow; this adversely affects the solution of fluctuating airflow. Supposing that the surface fluctuating pressure is dominantly induced by hairpin vortex from the boundary layer, the fluctuating pressure values obtained from these two models are predetermined to be small. However, if the fluctuating pressure was mainly generated by a hairpin vortex from the tail flow area, the outcomes from both models approximate that from the LES.

Virtually, SAS is also a URANS model in nature and introduces the von Karman length scale based on the URANS model. This scale can self-adjust according to the local flow structure and dynamically modify the turbulent viscosity depending on the flow pattern [30]. The SAS can accurately imitate eddies of various scales in the mainstream domain. In addition, it can visualize the dynamic revolution of an eddy according to the known flow field in the present boundary layer and dynamically adjust the length scale to realize simulating fluctuating airflow by using a large eddy model. Compared to the DES model, SAS does not have the interface problems between the two computing regions of URANS and LES, and of course, SAS does not need to divide the computational domain into the URANS and LES computing regions through the grid scale, which opens a new way to simulate the fluctuating flow field. Nevertheless, this model may be unstable for solving the numerical simulation problem caused by weak high-wave number dissipation in practice. This instability is attributed to the fact that the mesh is not competent in ensuring the generation of sufficiently small turbulent viscosity through the von Karman length scale to produce small-scale eddy. As a result, the transfer path of turbulence kinetic energy is interrupted from large to small-scale eddy. The high-wave number turbulence kinetic energy accumulates owing to the absence of dissipation; this in turn poses a negative effect on the numerical computation. In addition, the capacity of modelling a SAS flow-field structure is positively correlated to the airflow instability.

3. Discussions of Simulation Performance of Turbulent Models on Cylinder Aeroacoustics

A cylindrical structure is common in engineering applications. The eddy sheds alternatively at the wake zone when fluid media flow through its surfaces at a certain range of the Reynolds number. The formed vortex street is then imposed on the cylindrical surface, forming fluctuating pressure and generating a wide band noise of certain peak frequencies [31]. The performance of cylindrical turbulence with high

nautical numbers calculated by different turbulence models can reflect the degree of the turbulence model to calculate the quality of the pantograph flow field.

Figure 1 illustrates the calculation model of a cylinder, in which the inlet was set as velocity, outlet as pressure, upper surface $z1$ and bottom surface $z2$ as velocity inlets, and left surface $y1$ and right surface $y2$ as symmetric boundaries. Diameter d and span length of the cylinder are 19 mm and 10 d, respectively, the inflow velocity was 69.19 m/s, and the Reynolds number was approximately 90,000.

ICEMCFD (Integrated Computer Engineering and Manufacturing Code for Computational Fluid Dynamics) is professional CAE preprocessing software, which can provide reliable analysis model. The piecewise meshing method in ICEMCFD was implemented to discretize the calculation domain into a hexahedron, the number of which was approximately 11 million. The mesh size of the cylinder includes a circumference and span of 0.2 and 1 mm, respectively, and its maximum size is 2 mm in other regions. For better comparisons, the meshes of the five turbulent models in mainstream zone are the same except for the thickness of the first layer near the cylindrical surface; this depends on each individual's y plus value [32]. The optimal y plus value for the LES model should be less than 1. For the 0.006-mm-thick first layer, the value of y plus is approximately 0.6. Likewise, the 0.08-mm-thick first layer corresponds to a y plus value of 10.2, which is also approximately close to its recommendation value of 10. Furthermore, the orthogonality optimization was applied to the boundary layer and wake flow area of the cylinder to obtain highly orthogonal meshes. Figure 2 shows the mesh on the span intersection.

Virtually, the aeroacoustic simulation of a cylinder is much more analogical to that of a pantograph [33]. The differences lie in the fact that the sst-kω model is used for steady turbulence, instantaneous time-step $\Delta t = 2 \times 10^{-5}$ s, and the total computation time for the transient flow field is 6000 steps, of which the former 1000 steps are used to confirm sufficient revolution of turbulent flow field, while the remaining steps are used for extracting sound-source information.

3.1. Flow-Field Structure. Previous research revealed that the flow field of a cylinder is unsteady under a Reynolds number of 90,000, representing the turbulent vortex street of laminar-turbulent separation [31]. The transient contours of the vorticity amplitude of the five models in the simulated cylinder-span intersection are displayed in Figure 3 and measured in s^{-1}. Figure 4 shows the isosurfaces of the five models at $Q = 2{,}000{,}000$ rendered by the colour chart in Figure 3.

In contrast, the transient flow fields obtained from the five models in Figures 3 and 4 are very close. The subtle structures of the shedding eddies together with their born alternatively distributed vortex street structures can be captured at the process of propagation in wake flow. In addition, the intensive vorticity airflow separated from the cylinder even the small-scale halfer hairpin vortex whirled

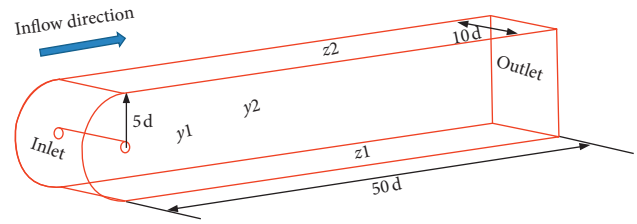

Figure 1: Computation domain for the cylindrical turbulent flow.

by middle-large-scale halfer hairpin vortex among the vortex street is obtained. However, the airflow-separation positions, propagation speed and size of vortex streets in longitude, intensity, and scales vary considerably between the five models.

The separation angles calculated by the five models are 81.8°, 85.5°, 88.2°, 88.7°, and 105.6°, respectively. The time-averaged results of aerodynamic drag coefficient calculated by the five models are 1.23, 1.14, 1.13, 1.11, and 0.61. It is shown that the airflow-separation position obtained using the DDES R-kε model lags those obtained using the other models, and the aerodynamic drag coefficient is much smaller than the experimental result of 1.2 [31].

Regarding the longitudinal propagation velocity of the vortex street, the results derived from DDES R-kε are significantly lower than those from other models, indicating that the peak aerodynamic lift force is small. Actually, the peak forces from the five models are 2.61, 1.80, 0.77, 1.12, and 0.34, respectively, indicating a lower result from the DDES R-kε than from the other models.

Additionally, DDES R-kε is less superior in calculating the size, intensity, and scale of hairpin eddy groups at the wake-flow area, suggesting its disadvantage in modelling the hairpin eddy groups. This is mainly because DDES R-kε overestimates the turbulent viscous coefficient in the upstream of the cylinder, thus reducing the LES's ability to capture the downstream vortices. Interestingly, the shapes obtained from the modelling of hairpin eddy groups by using DDES R-kε, DDES sst-kω, IDDES sst-kω, and LES are similar with respect to the sufficient revolution areas of wake flow which is 15 d far from the cylinder axis in the downstream area. Nonetheless, the scale of the eddy group obtained using the LES is larger than those using DDES R-kε, DDES sst-kω, and IDDES sst-kω, denoting that the latter models have a significant grey-zone effect. The size of modelled hairpin eddy by using the SAS is larger than those obtained through other models representing its inferiority in calculating small-scale hairpin eddies, especially in the sufficient revolution area of the wake flow. In other words, SAS performs poorly in the modelling of a small-scale vortex structure in the steady flow area.

Overall, among the five turbulent models, LES ranks the most excellent in simulating the cylinder-based fluctuating flow field followed by SAS, DDES sst-kω, and IDDES sst-kω, while DDES R-kε performs the worst.

3.2. Aeroacoustic Sound Source. The derivative of surface fluctuating pressure to time p' can represent sound source

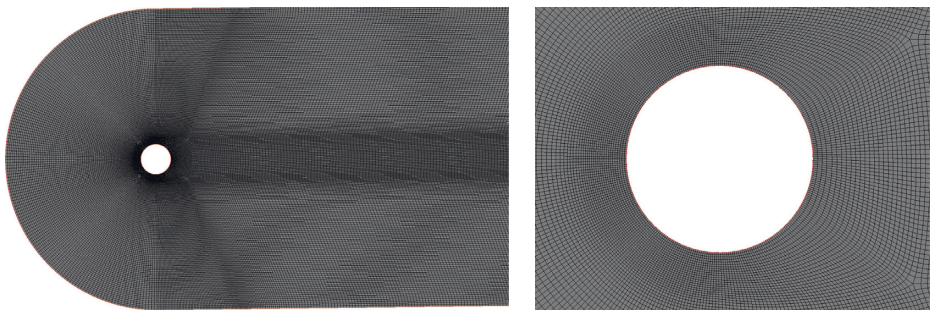

(a) (b)

Figure 2: Middle intersection mesh on the radial direction of the cylinder: (a) the global mesh; (b) the locally enlarged mesh near a cylinder.

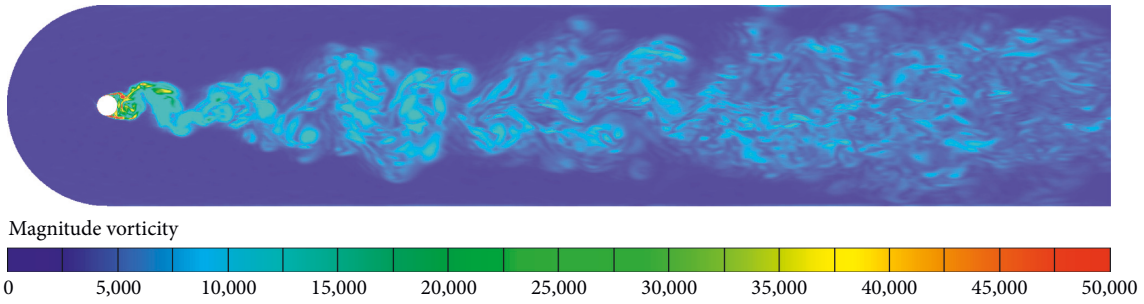

(a)

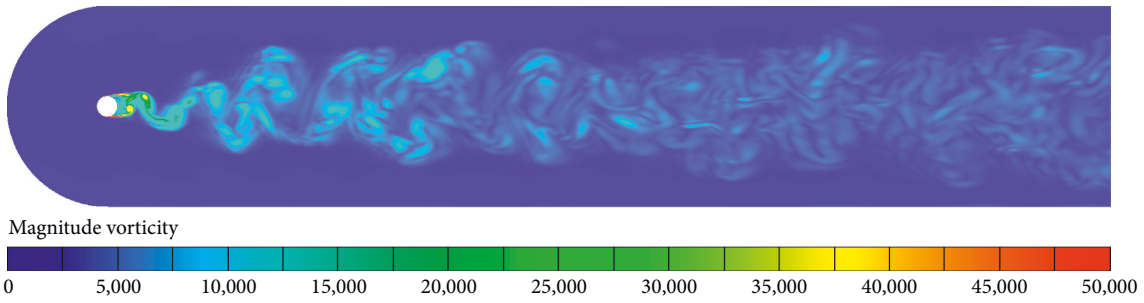

(b)

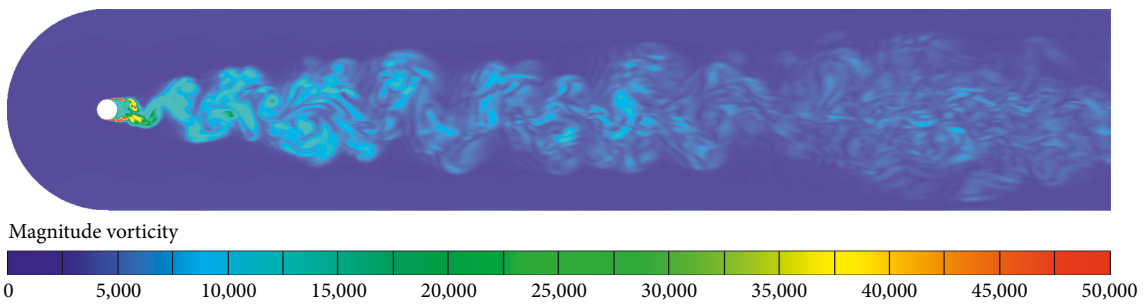

(c)

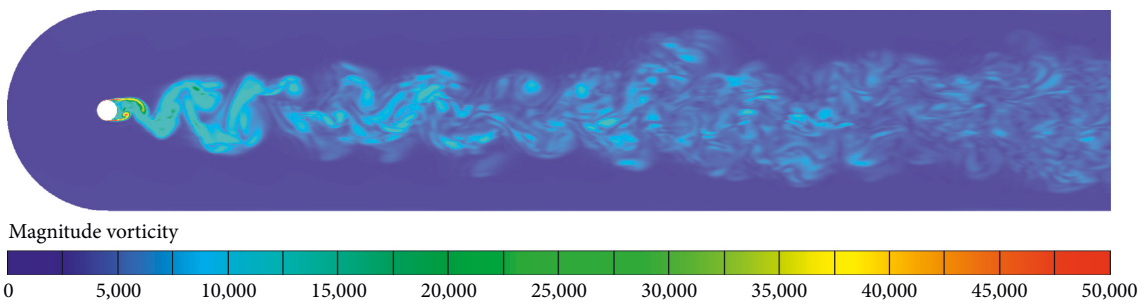

(d)

Figure 3: Continued.

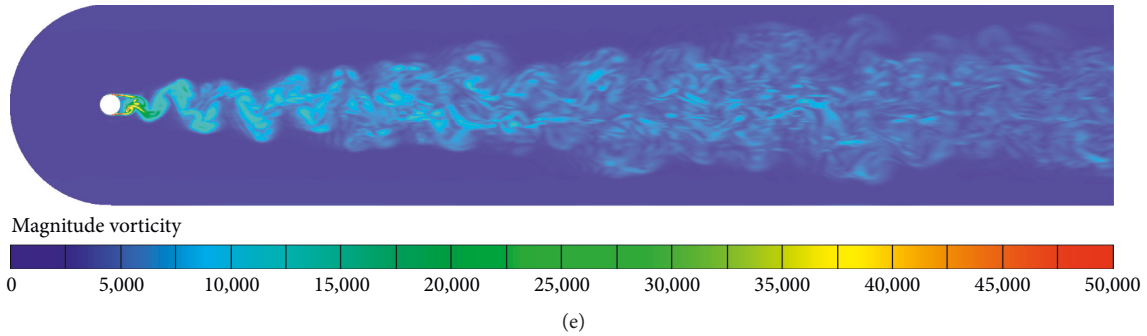

Figure 3: Cylindrical vorticity amplitude of the five models: (a) LES, (b) SAS, (c) IDDES sst-kω, (d) DDES sst-kω, and (e) DDES R-kε.

intensity [33]. Here, p' was used to evaluate the performances of the five models in simulating the aeroacoustic source of a pantograph. Root mean square p'_{rms} of p' is defined using Equation (1) to represent the average of the sound-source intensity within sample time. Figure 5 exhibits the differences between the values of p'_{rms} for the five models, qualitatively:

$$p'_{\text{rms}} = \sqrt{\frac{1}{T}\int_0^T (p')^2 dt}, \tag{1}$$

where T is the sample time length.

Figure 5 shows that the distribution characteristics of p'_{rms} of the five models are more coincidental while bias greatly in amplitude. Explicitly, the results of p'_{rms} downwind from the five models are larger than that upwind; however, the values calculated using LES and SAS are larger than those obtained through the other models, among which DDES R-kε produces the lowest value.

To quantitatively analyse the discrepancy of W_{source} [33], it should be calculated using Eq. (2) to obtain the root mean square of the gradient of fluctuating force F'_{rms}; this is then substituted into Eq. (3) to generate an equivalent sound power W_{source} and is finally used to calculate the percentage of other models standardized using W_{source} of LES, as shown in Figure 6:

$$F'_{\text{rms}} = \int_s p'_{\text{rms}} ds, \tag{2}$$

where s is the area:

$$W_{\text{source}} \propto \overline{F'^{\,2}_{rms}}. \tag{3}$$

According to Figure 6, the results of SAS, DDES sst-kω, IDDES sst-kω, and DDES R-kε are 9.2, 12.3, 11.9, and 19.5 dB less than that of LES, respectively. By referring to Figure 5, it can be inferred that the downwind surface results in smaller values from SAS, DDES sst-kω, IDDES sst-kω, and DDES R-kε, in order.

To determine the frequency ranges underestimated using SAS, DDES sst-kω, IDDES sst-kω, and DDES R-kε, Fourier transformation was conducted on W_{source}. The procedure of the algorithm is as follows. Extract the surface fluctuating pressure p in the time domain, apply Fourier transformation (1/3 octave) on p, and obtain P. Next, obtain surface fluctuating pressure gradient P' and fluctuating force gradient F' by using Eqs. (4) and (5), respectively, and calculate equivalent sound-source power W_{source} by using Eq. (3):

$$p' = 2\pi f P, \tag{4}$$

$$F' = \int_s P' ds, \tag{5}$$

where P is the physical variable of p through Fourier transformation [Pa], f is the frequency [Hz], F is the fluctuating force [N], s is the area of the train-body surface [m^2], and the right superscript represents the derivative to time.

Figure 7 illustrates the percentage of W_{source} for the five models at different frequencies standardized by the result of LES.

Figure 7 shows that the SAS result is slightly larger than that of LES at the centre band frequency of 800 Hz and less than that of LES elsewhere. The results of IDDES sst-kω, DDES sst-kω, and DDES R-kε are all less than that of LES at full band, with DDES R-kε displaying the least result. The peak frequencies calculated using SAS, IDDES sst-kω, and DDES sst-kω are the same at 800 Hz, which is larger than that of LES with a value of 630 Hz. Moreover, the peak frequency of DDES R-kε is 1250 Hz, which is nearly two times larger than that of LES.

Overall, the results computed using SAS, IDDES sst-kω, DDES sst-kω, and DDES R-kε tend to be smaller compared with that of LES mainly because of their underestimation of W_{source} at the downwind area. IDDES sst-kω, DDES sst-kω, and DDES R-kε downplay W_{source} at full band, especially at high frequencies over 1000 Hz, while SAS generates slightly larger values than LES at the centre band frequency of 800 Hz and smaller values at other frequencies. Based on the performances at the full band, the computation accuracy decreases in the order of SAS, IDDES sst-kω, DDES sst-kω, and DDES R-kε.

3.3. Radiated Noise. The length of the cylinder in this paper is 10 d, and the length of the cylinder in reference [31] is 25 d. In reference [31], there is an end effect at both ends of the cylinder, but the middle (a length of 10 d) of the test cylinder is hardly affected by the end effect. Because the two ends of the cylinder in this paper are velocity entrances, there is almost no end effect on the cylinder in this paper, which ensures that the flow field simulated in this paper can be

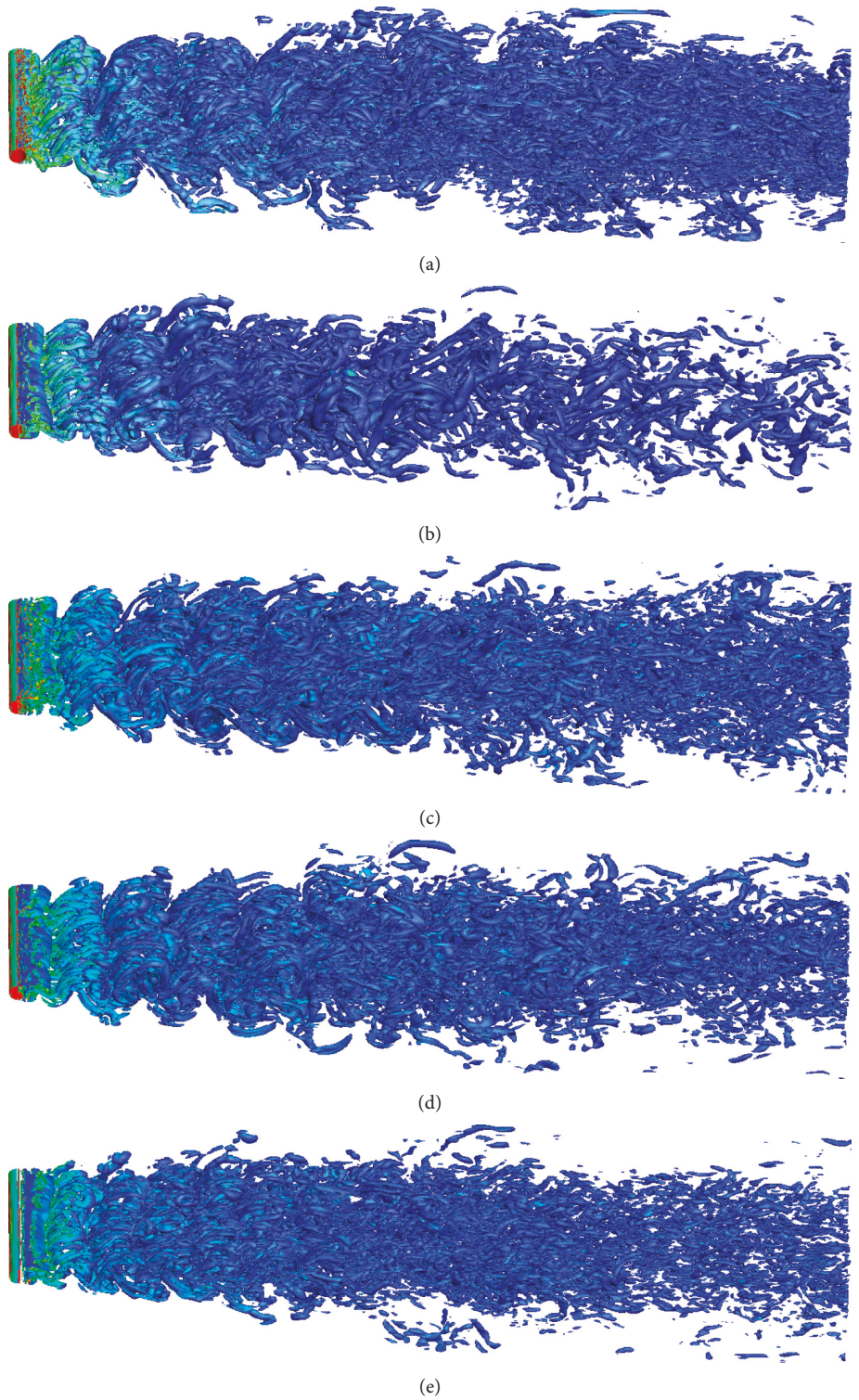

Figure 4: Instantaneous vortex structure of the cylindrical turbulent models of (a) LES, (b) SAS, (c) IDDES sst-kω, (d) DDES sst-kω, and (e) DDES R-kε.

consistent with that of the middle (a length of 10 d) of the test cylinder. Regarding the far-field radiated noise at 128 d from a far-right position over the cylinder, the outcomes of the five models were compared with that of Revell's experimental data [31], as displayed in Figure 8 and Table 1.

Figure 8 and Table 1 show that the SPL of LES is the closest to the experimental data, followed by that of SAS, whose relative errors are within 2%. IDDES sst-kω and DDES sst-kω have less than 10% errors; this is acceptable for engineering requirements. However, DDES R-kε scarcely reaches such

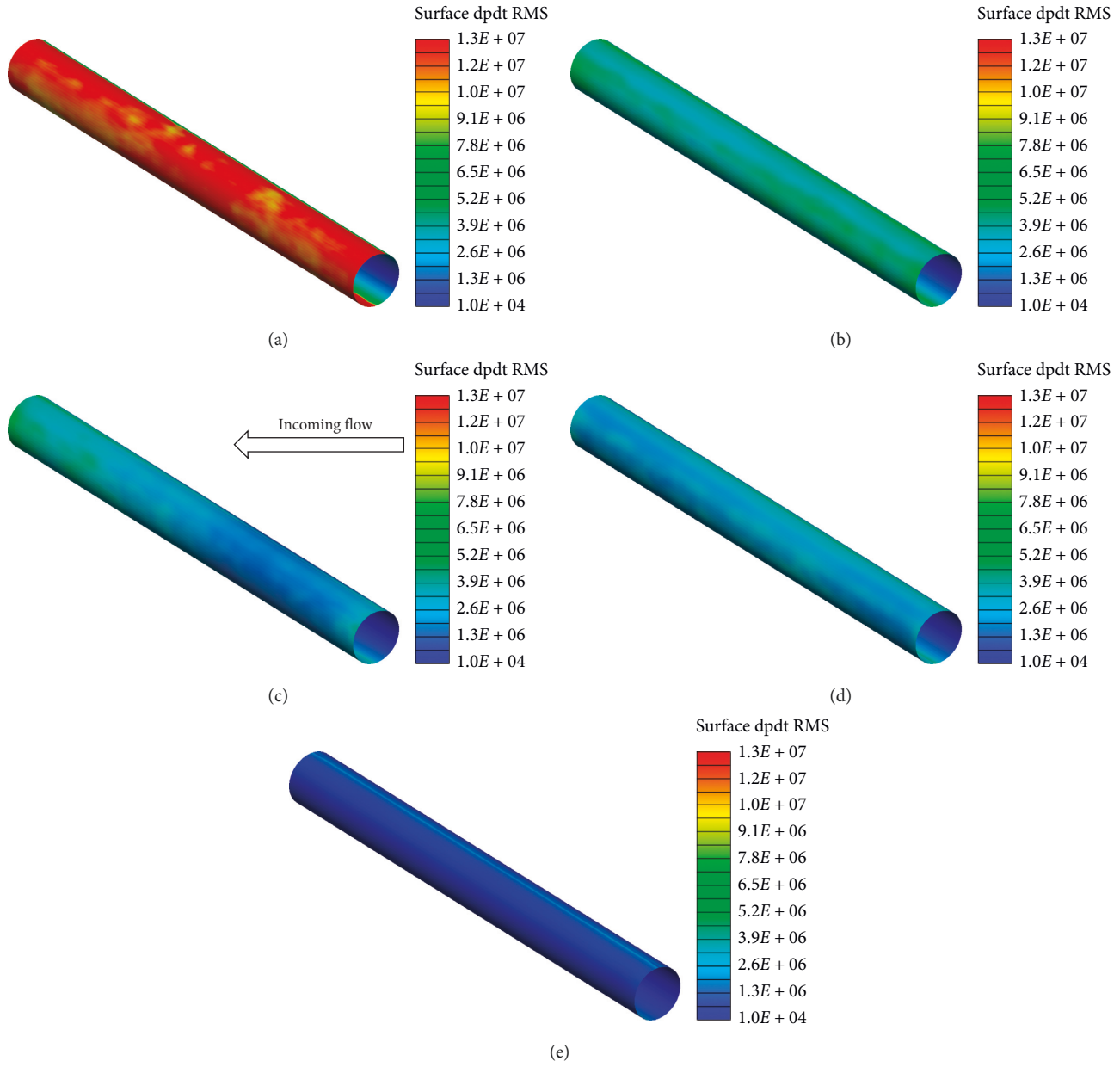

Figure 5: Distribution of p'_{rms} on the cylinder surface of (a) LES, (b) SAS, (c) IDDES sst-kω, (d) DDES sst-kω, and (e) DDES R-kε.

requirements as it shows large errors. With respect to the peak Strouhal number, LES provides the most accurate result followed by IDDES sst-kω, while SAS and DDES sst-kω narrowly meet the engineering requirements; DDES R-kε fails to meet these requirements. From the perspective of aeroacoustic frequency spectrum, the curves of the five models lie under the experimental curve; this is attributed to the mix of free-flow noise in the experimental setup [31]. Furthermore, the curves of LES, SAS, IDDES sst-kω, and DDES sst-kω beyond the peak Strouhal number have good agreement with the experimental curves, among which LES still shows great fit with the experimental data. In contrast, DDES R-kε shows the worst fit for the whole Strouhal number interval.

This suggests that LES possesses high accuracy in computing radiated noise of cylinder and SAS, IDDES sst-kω, and DDES sst-kω show a moderate performance. DDES R-kε could hardly meet engineering requirements.

3.4. Brief Summary. The adaptabilities of the five turbulent models in simulating aeroacoustics of cylinder from the aspects of flow-field structures, aeroacoustic source, and radiated noise were investigated. In addition, their performance evaluation was based on comparisons with experimental data. Considering the distinct discrepancy on airflow-separation position and the longitudinal propagation velocity of vortex street plus with the size, intensity, and scales of hairpin eddy group, the results obtained from the five models bias much in simulating aeroacoustic source; this directly results in a considerable difference in

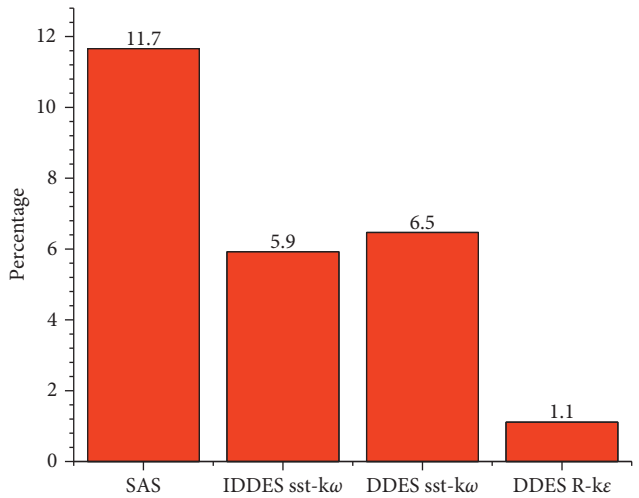

Figure 6: Percentage of the cylinder W_{source} of the four models relative to LES.

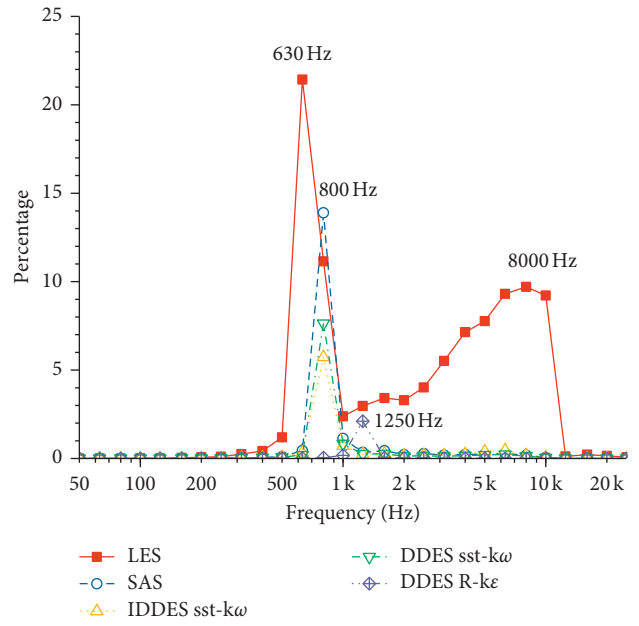

Figure 7: Frequency spectrum curves of W_{source} of the five models.

the aeroacoustics. Based on the computation accuracy of flow structure, aeroacoustic source, and radiated noise, the five models can be ranked from the best to worst as LES, SAS, DDES sst-kω, IDDES sst-kω, and DDES R-kε. Virtually, SAS, DDES sst-kω, and IDDES sst-kω, but not DDES R-kε, can work as substitutes for LES in simulating aeroacoustics of a cylinder, considering engineering accuracy.

Despite that the pantograph mainly comprises rods, the plate structure, which is mostly assembled at the bottom regions, cannot be ignored. Xiao-Ming et al. [33] highlighted that the bottom region of a pantograph is a major noise source. Hence, the competency of SAS, DDES sst-kω, and IDDES sst-kω with LES in simulating aeroacoustics of a pantograph still requires further investigation.

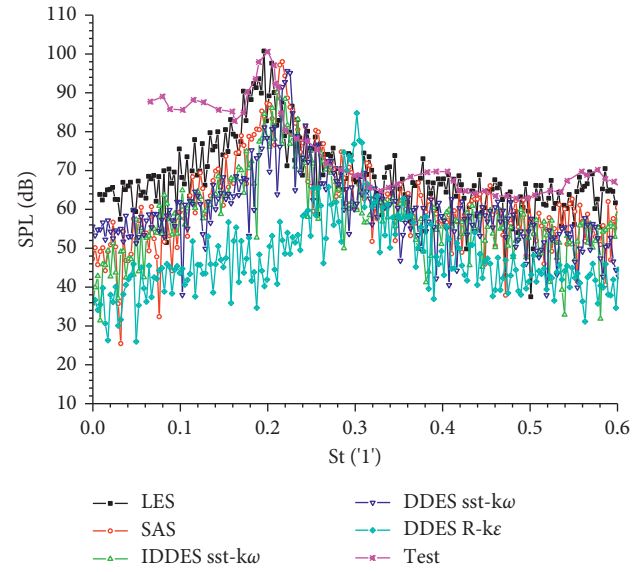

Figure 8: Aeroacoustic frequency spectrum curves of the five models at 128 d far-right position over the cylinder.

4. Discussions of Simulation Performance of Turbulent Models on Pantograph Aeroacoustics

As this paper is developed from another paper of the author [33], the refined aerodynamic noise simulation technology of pantograph is not introduced in detail in this paper. It should be noted that the mainstream grids used in the five turbulence models are exactly the same, and the thickness of the first layer near the cylinder is determined only according to the YY + principle. For ease of description, Figure 9 gives the geometric model of pantograph and the naming of each part. In this study, the pantograph was cut into 23 parts classified into 3 areas: the panhead, middle, and underframe areas. The panhead area includes horn 1, horn 2, horn support 1, horn support 2, panhead, panhead knuckle 1, panhead knuckle 2, panhead support 1, panhead support 2, balance beam, supporting frame 1, and supporting frame 2. The middle area includes the arm knuckle, rod, balance rod, upper arm frame, and lower arm. The remaining components were classified as the bottom frame area.

Although we know that DDES R-k is not suitable for simulating cylindrical aerodynamic noise, it may be evaluated together with other turbulence models to calculate the performance of the pantograph aerodynamic noise. Xiao-Ming et al. [33] discussed in detail the flow-field structure, aerodynamic noise source, and radiation noise characteristics of the pantograph at different inflow speeds, and the purpose of this study is to evaluate the performance of the pantograph aerodynamic noise according to the five aforementioned turbulence models. Therefore, this section only elaborates on the latter part.

4.1. Flow-Field Structure. The accurate computation of surface fluctuating pressure, which depends on accurate

Table 1: SPL and peak Strouhal number of the five models at 128 d far-right position over the cylinder.

	TEST	LES	SAS	IDDES sst-kw	DDES sst-kw	DDES R-kε
SPL (dB)	100.00	100.66	98.38	92.17	96.17	87.95
Relative error of SPL (%)	—	0.66	1.62	7.83	3.83	12.05
St_{max}	0.200	0.196	0.217	0.211	0.223	0.302
Relative error of St_{max} (%)	—	2.0	8.5	5.5	11.5	51.0

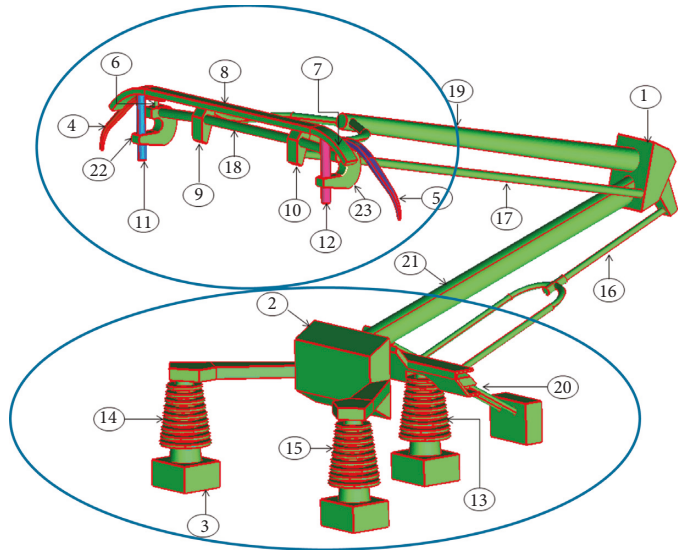

Figure 9: Geometric structure of the pantograph. 1: the arm knuckle, 2: the bottom frame, 3: the base, 4: horn 1, 5: horn 2, 6: horn support 1, 7: horn support 2, 8: the panhead, 9: panhead knuckle 1, 10: panhead knuckle 2, 11: panhead support 1, 12: panhead support 2, 13: the rod insulator, 14: supporting insulator 1, 15: supporting insulator 2, 16: the rod, 17: the balance rod, 18: the balance beam, 19: the upper arm frame, 20: the push/pull shaft, 21: the lower arm, 22: supporting frame 1, and 23: supporting frame 2.

simulation of the surrounding fluctuating flow field of pantograph, is critical in calculating its acoustic field. In general, it is necessary to consider the full-scale accuracy of zero- and first-order variables and capture the ability of vortex structures in determining the simulation accuracy of the fluctuating flow field. Vorticity is the curl of velocity or the linear function of the first-order derivative of velocity. The Q value shows the differences of squares between vorticity tensor and the two norm of strain-rate tensor; these can help identify the vortex structures around the pantograph. Thus, velocity amplitude, vorticity amplitude, and Q value are selected to assess the simulation accuracy of the five models. In addition, the statistical average of the velocity and vorticity amplitudes is applied for better assessment. The statistical sample time range is 0.05 s, covering a sample number of 1000.

Xiao-Ming et al. [33] revealed that the radiated noise energy from the bottom region of a pantograph accounts for 58% of the total noise. In this study, only the fluctuating flow field at the bottom region was discussed with respect to the five models. Figures 10 and 11 illustrate the average velocity amplitude and average vorticity amplitude contours at the isohypsic surface (the height from the ground is 0.32 m) of an insulator. I, II, and III are marked in Figure 10(a) for the convenience of flow-field structure analysis. In Figure 12, the isosurfaces of $Q = 10{,}000$ of the five models at the same instant are drawn, rendered by the velocity amplitude [m/s].

The five models, which can capture the generation and revolution history of a low-velocity zone, bias slightly in the average velocity amplitude but vary in precision. Zones I and II represent the wake flow area of the two supporting insulators, and zone III represents the wake flow of the pull rod insulator. In zones I and II, the shape of the low-velocity zone is calculated using LES presents waviness, which indicates the effect of periodical lateral force on the zones. In contrast, none of the other models captures this phenomenon. In zone III, a spindle is formed at the low-velocity zone close to the pull rod insulator, after which it is converted into small-piece low-velocity zones at the downstream end. As a result of the periodical lateral force, these small-piece zones gradually cover the whole wake flow area during their movement downstream. Evidently, DDES R-kε shows a slightly inferior performance to the other models in capturing this phenomenon.

Despite no significant differences in terms of average vorticity amplitude among the five models in capturing the generation and revolution history of an intensive vorticity zone, the models show varied abilities in capturing small-scale flow-field structures around the intensive vorticity zone. At the wake flow areas of the supporting insulators, LES, SAS, IDDES sst-kω, and DDES sst-kω can obtain wave-like intensive vorticity zones and recur the process of these zones' continuous separation from small-piece intensive vorticity zones. At the downstream area of the pull rod insulator, SAS shows obviously larger intensive vorticity

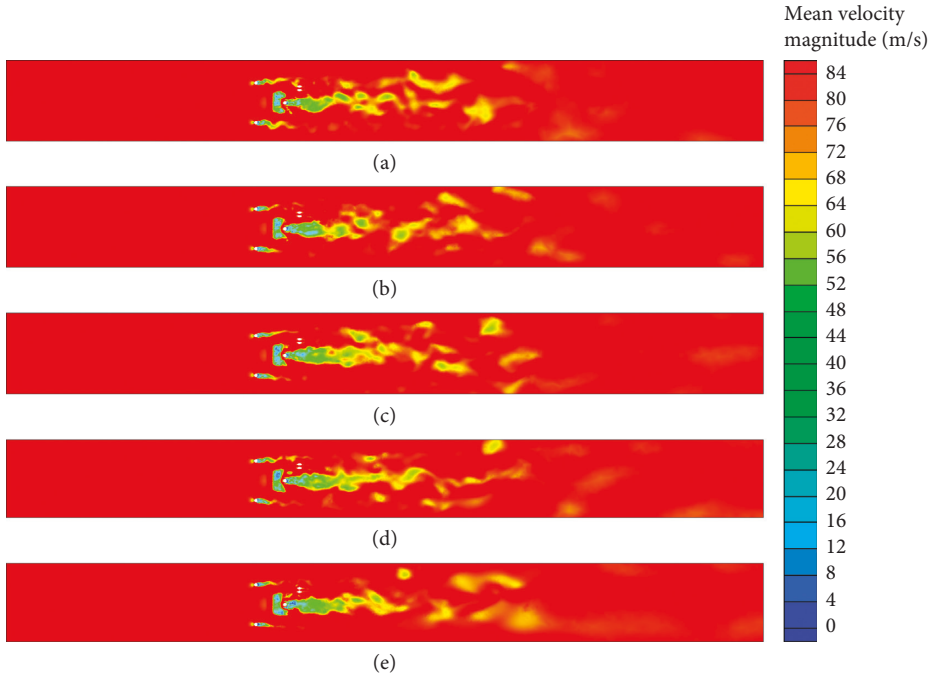

Figure 10: Average velocity amplitude of the pantograph using the (a) LES, (b) SAS, (c) IDDES sst-kω, (d) DDES sst-kω, and (e) DDES R-kε models.

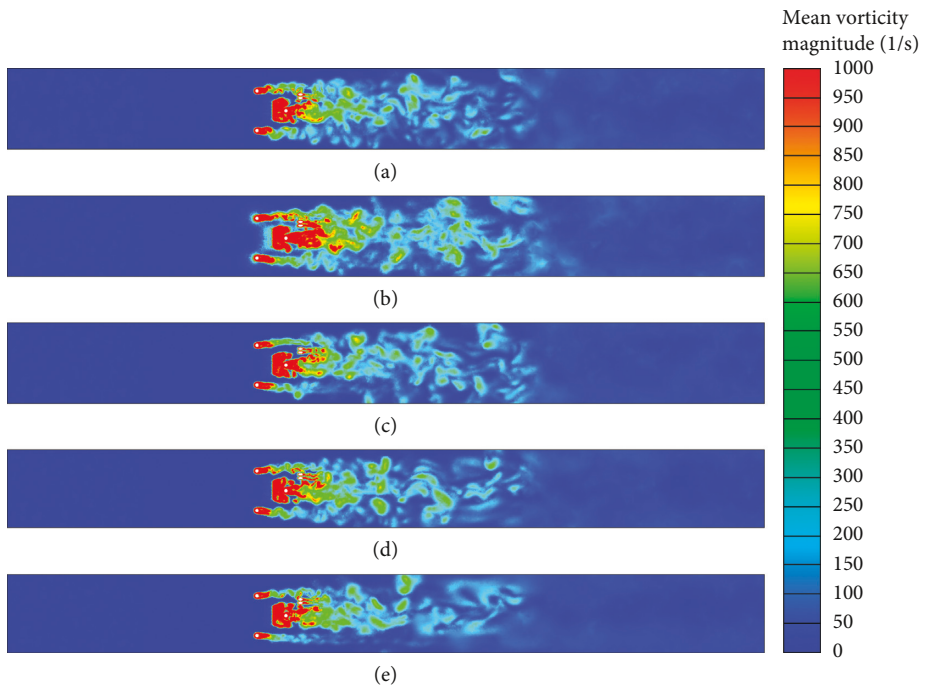

Figure 11: Average vorticity amplitude of pantograph using (a) LES, (b) SAS, (c) IDDES sst-kω, (d) DDES sst-kω, and (e) DDES R-kε models.

zones than other models and LES, IDDES sst-kω, and DDES sst-kω shows such zones in various geometric sizes. Nevertheless, DDES R-kε is unsatisfactory in capturing these flow fields.

With respect to the vortex structure of the instantaneous flow field, the five models show a closely similar characterizing trend. That is, the inflow experiences air-fluid separation when passing through the pantograph and bubble-like small-scale vortex structures are produced, which revolutionize into large-scale halfer hairpin eddy when moving downstream with the inflow. Obviously, the vortex structure distributes into three layers in space. The

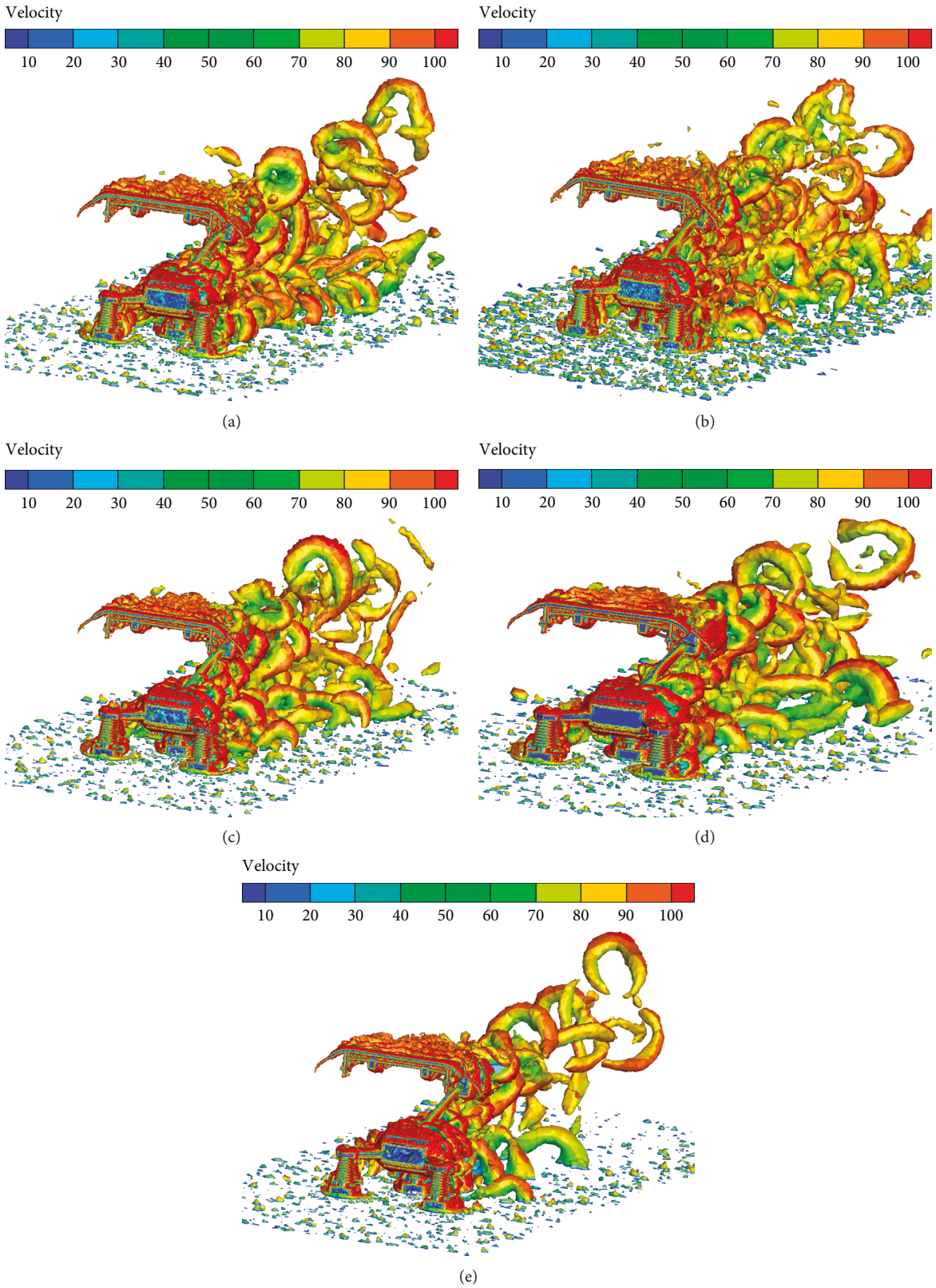

Figure 12: Instantaneous vortex structure of (a) LES, (b) SAS, (c) IDDES sst-kω, (d) DDES sst-kω, and (e) DDES R-kε models.

first of these layers originates from the underframe region of the pantograph, the second layer originates from the middle region, and the third layer originates from the panhead region. In addition, the first and third layers merge with the second layer moving downstream. However, the five models are distinct in the calculation precision of the vortex

structure. In detail, LES can not only cause the reappearance of the small-scale eddy structure but can also capture the sequential large-scale eddy structures at the wake flow of the three insulators. The ability of SAS to reproduce small-scale vortices is slightly stronger than LES. However, SAS does not capture orderly large-scale vortices. Further, IDDES sst-kω and DDES sst-kω show lower abilities than LES in capturing small-scale eddy structure but can rarely capture large-scale eddy structures. At the wake flow, DDES sst-kω shows a greater ability than the other models in modelling large-scale eddy structures, whereas DDES R-kε is inferior to other models in the modelling of either small-scale or sequential eddy structures.

In conclusion, LES has the best performance in simulation precision of fluctuating flow field followed by SAS, DDES sst-kω, and IDDES sst-kω, while DDES R-kε ranks the worst. On this basis, it is supposed that the computation results obtained from LES are credible under the condition of limited test data. Hence, we will evaluate other the computation accuracies of other models in comparison with that of LES.

4.2. Aeroacoustic Source. A pantograph strongly interferes with the inflow air, consequently generating varying scales of eddies. These eddies react on the surface of the pantograph causing fluctuating pressure during their formation, shedding, and breaking. Figure 13 exhibits the qualitative difference in the distribution of p'_{rms} among the models.

Figure 13 shows that the models are consistent in the distribution characteristics of p'_{rms} but are biased in magnitude. For example, all the models can verify that p'_{rms} in the downwind direction is larger than that in the upwind direction for the two supporting insulators. Nevertheless, LES and SAS results are significantly larger than those of other models, among which DDES R-kε produces the least satisfactory result.

By nominating W_{source} from LES, the percentages of other models were calculated, as shown in Figure 14. Moreover, the percentage of the four models nominated by LES is tabulated in Table 2 classified by the panhead, middle, and underframe regions.

Figure 14 and Table 2 show that the results of SAS, IDDES sst-kω, DDES sst-kω, and DDES R-kε are 4.6, 6.9, 9.4, and 12.9 dB lower than that of LES, respectively, considering W_{source} of the whole pantograph. In the case of W_{source} of the bottom region, they are 5.8, 9.4, 13.4, and 16.0 dB lower than that of LES; for the middle region, they are 2.4, 3.1, 4.9, and 9.1 dB, and for the panhead region, they are 1.7, 3.8, 4.8, and 7.7 dB lower than that of the LES, respectively. As revealed in Reference [33], W_{source} of the bottom region accounts for 71% of the total pantograph. Consequently, the reason for smaller results of SAS, IDDES sst-kω, and DDES sst-kω lies in the bottom region, especially at the three insulators and their base. Notably, DDES R-kε negatively undervalues W_{source} of almost all pantograph components.

To determine the frequency range underestimated by SAS, IDDES sst-kω, DDES sst-kω, and DDES R-kε, Fourier transformation is applied to W_{source}. The procedure of the calculation is as follows. First, extract the time-domain signals of surface fluctuating pressure p of the pantograph from the flow field, then exert Fourier transformation (1/3 octave) onto p to produce P. Next, calculate surface fluctuating pressure gradient P' and fluctuating force gradient F' using Equations (4) and (5), respectively, and obtain equivalent acoustic source power W_{source}.

By nominating W_{source} with results from LES at each frequency, the percentage of the four models is obtained, as shown in Figure 15.

As illustrated in Figure 15(a), SAS, IDDES sst-kω, DDES sst-kω, and DDES R-kε produce smaller results than LES at full-band frequencies for the whole pantograph, among which DDES R-kε generates the least. Obviously, the computation precision of SAS within the range of 1000–3150 Hz is less satisfactory than others. In addition, IDDES sst-kω, DDES sst-kω, and DDES R-kε severely underestimate W_{source} at frequencies over 800 Hz. Overall, the computation precision of W_{source} decreases in order of SAS, IDDES sst-kω, DDES sst-kω, and DDES R-kε for the whole pantograph at full-band frequencies.

Figure 15(b) shows that the results of W_{source} for IDDES sst-kω, DDES sst-kω, and DDES R-kε are lower than that for LES at the underframe region at full-band frequencies (especially, for frequencies over 800 Hz). Moreover, the SAS result is lesser than that of LES at frequencies below 1000 Hz but contradictory over 1000 Hz. These diversities reflect their differences in modelling the vortex structures of wake-flow areas of underframe regions, validating the generality that a smaller size of eddy corresponds to higher frequency of source. It can be exemplified that the scale of small-scale vortex structure modelled using the SAS at the wake flow in the underframe region is larger than that modelled using LES, while smaller for large-scale vortex structures, this results in larger W_{source} by using SAS at high frequencies and smaller at low frequencies.

In summary, SAS, IDDES sst-kω, DDES sst-kω, and DDES R-kε produce low W_{source} for the whole pantograph compared with LES because of their underestimation of W_{source} in the underframe region. IDDES sst-kω, DDES sst-kω, and DDES R-kε undervalue W_{source} of the whole pantograph at full-band frequencies, especially at high frequencies over 800 Hz. SAS underestimates W_{source} in the underframe region at frequencies below 1000 Hz and overestimates it at frequencied of more than 1000 Hz. Based on their computation precision at full-band frequencies, the four models are ranked in the order: SAS, IDDES sst-kω, DDES sst-kω, DDES R-kε.

4.3. Radiated Noise. In addition to the image-forming principal, the integral of FW-H equation can be used to calculate the far-field radiated noise at ground effect; the detailed steps are as follows. First, create a couple of receptor points symmetrically about the ground and calculate their time-domain signal according to the integral of the FW-H equation, and then, add them to obtain the ground-effect-combined time-domain signal. Finally,

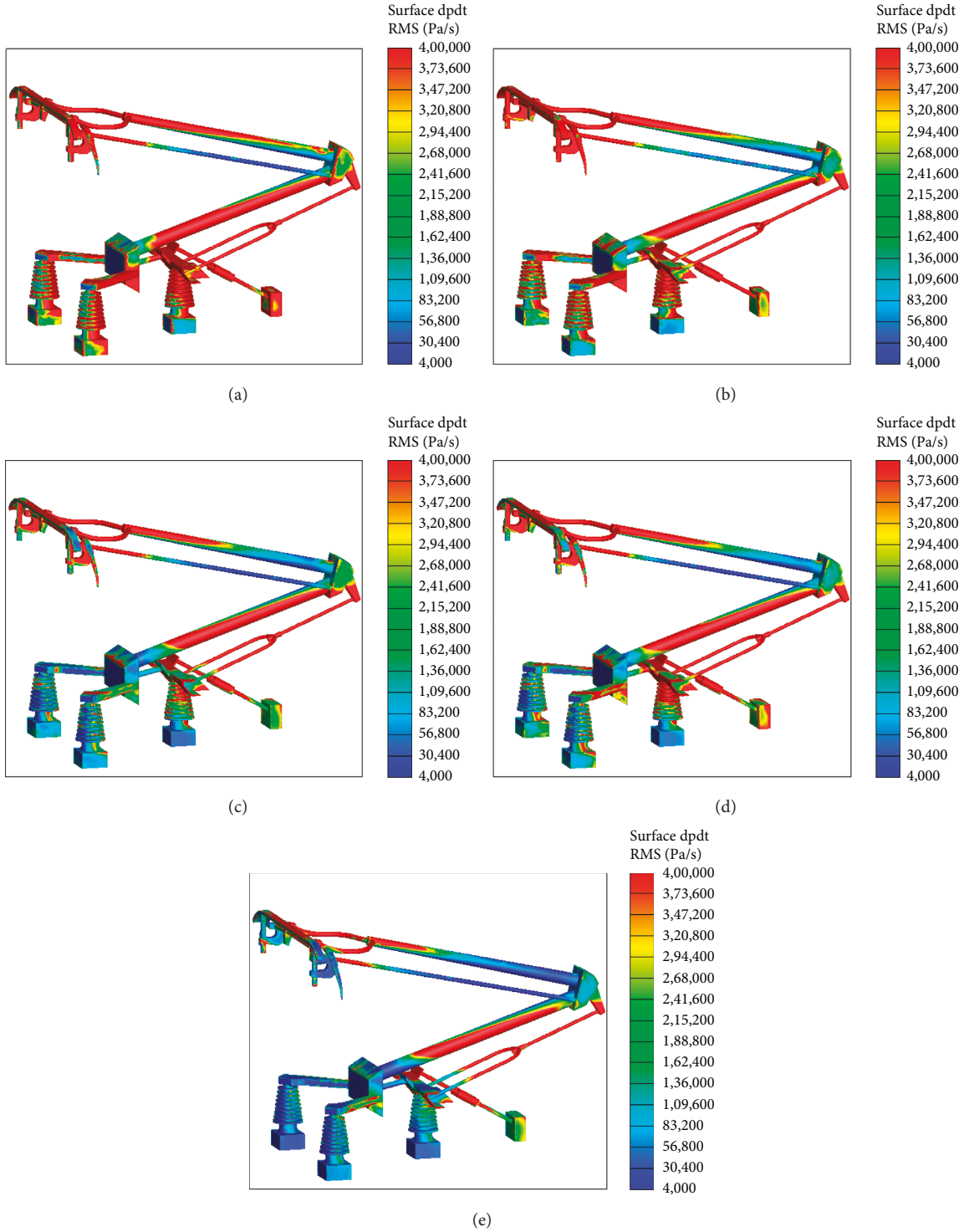

FIGURE 13: Distribution contours of p'_{rms} of pantograph surfaces for (a) LES, (b) SAS, (c) IDDES sst-kω, (d) DDES sst-kω, and (e) DDES R-kε models.

analyse the signal to explain their frequency spectrum characteristics of SPL.

Figure 16 shows the schematic of the pantograph receptor points. The projection coordinates of the geometric centre of the pantograph onto the ground are (0, 0, 0) m and the diameter of the circle is 280 m, with its centre at (0, 0, 0) m. The noise receptors are distributed every 10° to describe the directionality of the radiated noise of pantograph on each plane; the coordinate of the standard receptor point is (0, 25, 3.5) m.

With respect to the equivalent radiated acoustic energy density of the standard observation points, the percentage of

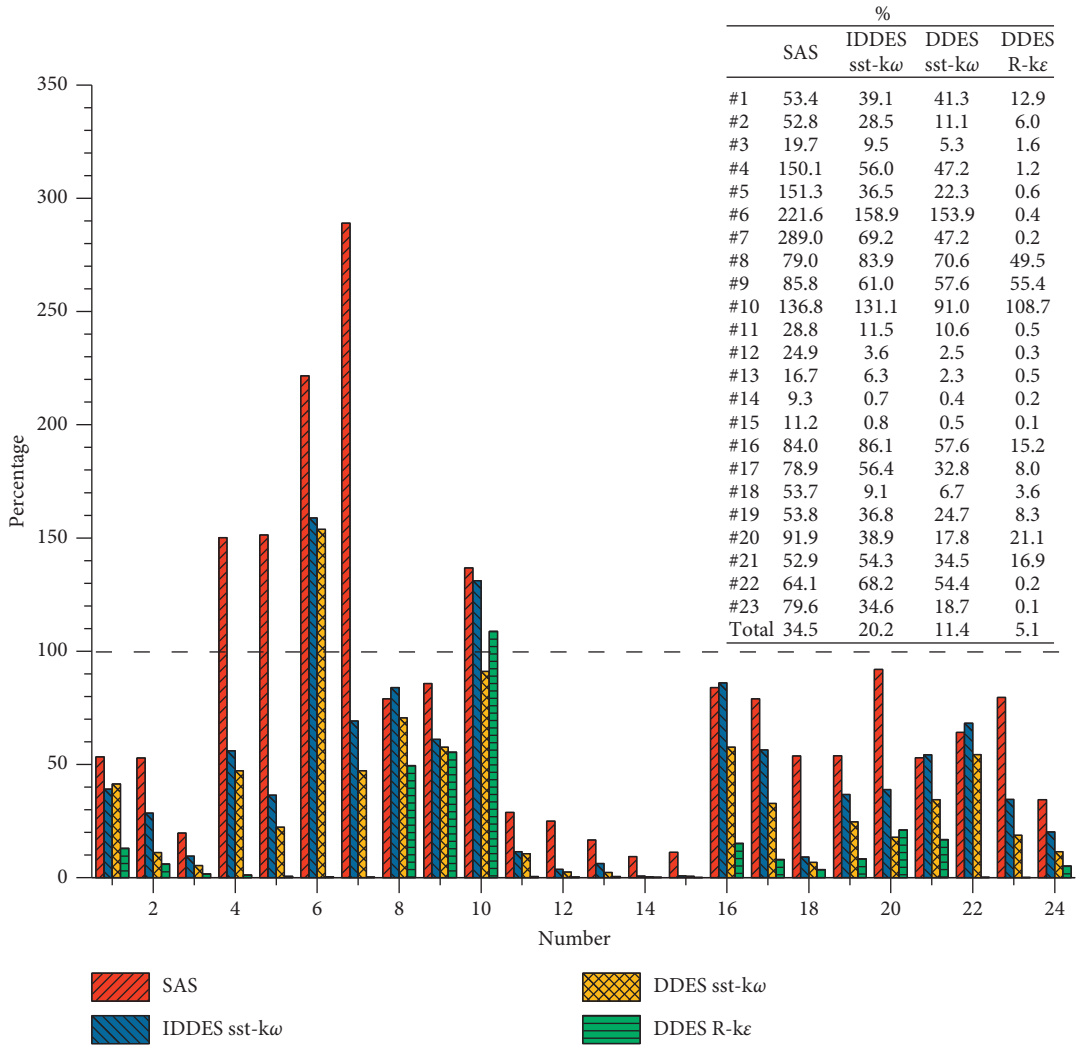

Figure 14: Percentage of W_{source} of the four models relative to LES for the whole pantograph and its components (350 km/h). The dashed line is a datum line representing the result from LES; the form represents the statistics of the components of the pantograph; the numbers coincide with those in Figure 9, and No. 24 represents the statistics for the whole pantograph.

Table 2: Percentage of W_{source} of the four models relative to LES (unit: %).

	SAS	IDDES sst-kω	DDES sst-kω	DDES R-kε
Bottom frame area	26.4	11.4	4.6	2.5
Middle area	57.4	49.4	32.7	12.4
Panhead area	66.9	41.4	33.1	16.9

the other models is as shown in Figure 17. These were obtained by employing the result from LES as nomination. The far-distance sound energy density I is also defined as

$$I = 10^{SPL/10}, \quad (6)$$

where SPL is the sound pressure level.

Compared with the LES result, Figure 17 shows that DDES R-kε severely underestimates the effect of underframe, middle, and panhead regions, especially the underframe region, which shows the smallest result. Despite better results than DDES R-kε, DDES sst-kω shows slightly larger results at the panhead region but much smaller results at the middle and underframe regions; this leads to an overall smaller result of the pantograph. Likewise, the results at the panhead, middle, and underframe regions are increasingly biased for IDDES sst-kω but are better than those of DDES sst-kω. SAS, which produces smaller value for the whole pantograph, shows the best fit with LES despite its larger result at the panhead region and smaller results at the middle and underframe regions. This indicates that the four models SAS, IDDES sst-kω, DDES sst-kω, and DDES R-kε, in order, show declining precision in computing acoustic energy density.

To confirm the frequency range of the underestimated equivalent radiated acoustic energy density, which is calculated using Equation (6), Fourier transform was applied to the obtained time-domain acoustic pressure of the standard observation points. The radiated aeroacoustic frequency spectrum curves of the standard observation points for the five models are illustrated in Figure 18. Figure 19 shows the percentage of the four models using the LES results at each frequency.

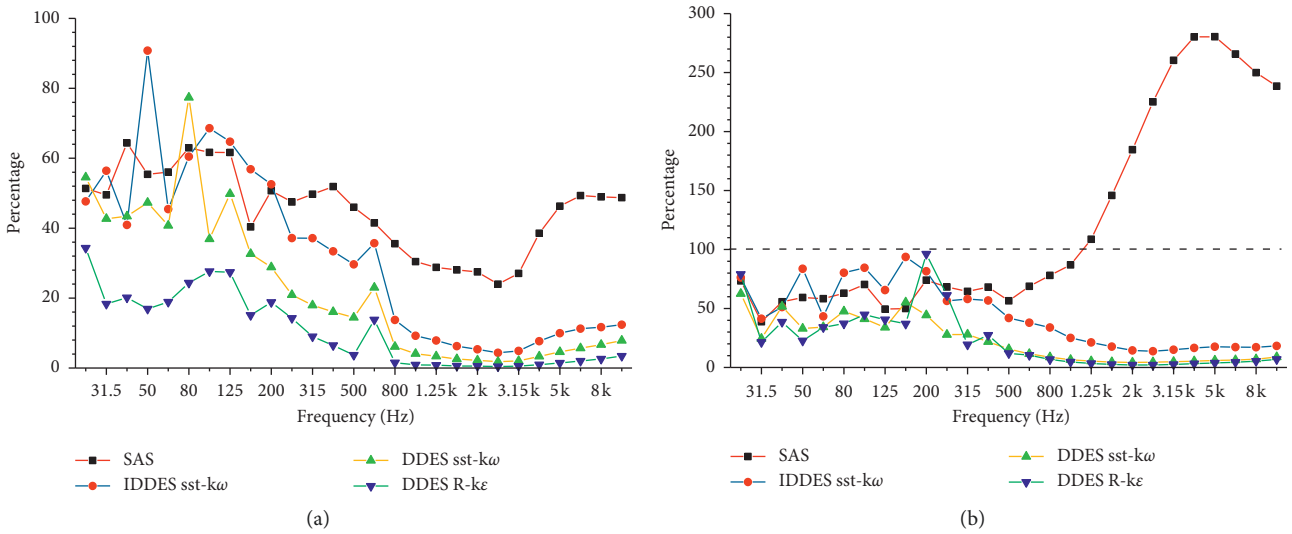

Figure 15: Percentage of W_{source} of the four models at all frequencies relative to LES (350 km/h): (a) whole pantograph and (b) bottom frame area. The dashed line represents the result from LES.

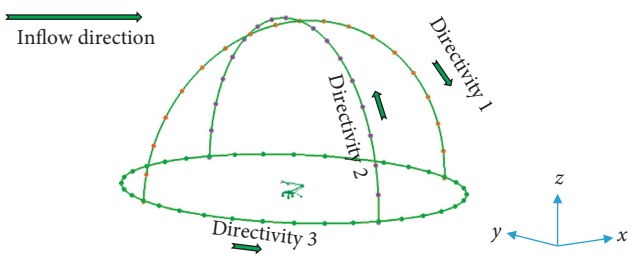

Figure 16: Schematic of the far-field noise-receiving points of pantograph.

As shown in Figure 18, at the standard receptor point, the curves of radiated noise frequency spectrum for the five models are characterized by small values at both ends and a large value at the middle; however, the curves vary considerably in SPL with respect to frequency. For example, the results from SAS, IDDES sst-kω, DDES sst-kω, and DDES R-kε are 1, 4, 7, and 10 dB, respectively, lesser than that of LES at frequencies higher than 1000 Hz. According to Figure 19(a), the comparison of the equivalent radiated acoustic energy density of the whole pantograph at the standard observation point from the four models with that of the LES shows that a higher result for DDES R-kε is only located where the centre frequency is 50 Hz. DDES sst-kω shows a higher result at bands with centre frequencies of 25 and 50 Hz, equalized result at bands with centre frequencies of 200 and 630 Hz and lower elsewhere. IDDES sst-kω shows equal result at frequency bands with centre frequencies of 63, 200, and 630 Hz; however, it shows lower result at most frequency bands. SAS produces higher result at some frequency bands with centre frequencies of 50, 63, and 200 Hz; lower result at bands, such as 40, 100, and 160 Hz; and balanced results at most frequency bands. It is conclusive that SAS has the closest outcome with LES followed by IDDES sst-kω, DDES sst-kω, and DDES R-kε in sequence.

Furthermore, the equivalent radiated acoustic energy density is analysed at the underframe region for the standard observation points, as is illustrated in Figure 19(b). Compared with LES, it is significant that IDDES sst-kω, DDES sst-kω, and DDES R-kε have smaller values but SAS generates better result at frequencies over 250 Hz, while the four models have approximate results at frequencies lower than 63 Hz.

The far-field directionality of radiated noise is compared in Figure 20. As is shown in Figures 20(a) and 20(b), the curves indicate a uniform consistency and shape like a half Arabic 8, which represents characteristics of the dipole noise source. Further, the directionality of IDDES sst-kω gets much close to that of LES in the *yz* plane and SAS in the *xz* plane, and the main energy radiation direction of the pantograph in the *yz* and *xz* plane can be clearly seen. However, the result of DDES R-kε is lower than that of LES, and its curve fluctuates considerably with bad smoothness. Moreover, LES, SAS, IDDES sst-kω, and DDES sst-kω have heart-like shape, as shown in Figure 20(c), whereas the shape of DDES R-kε is analogical to a bulb.

Overall, results of SAS, IDDES sst-kω, DDES sst-kω, and DDES R-kε are smaller than that of LES for the whole pantograph, which mainly attributes to their underestimation of the radiated noise from the underframe. In detail, for the radiated noise from underframe region, IDDES sst-kω, DDES sst-kω, and DDES R-kε undervalue the noise at frequencies higher than 250 Hz and SAS at bands with centre frequencies like 40, 100, and 160 Hz. Considering the far-field directionality of radiated noise, DDES R-kε is less superior to LES, SAS, and IDDES sst-kω, which show equal results. On the basis of computation accuracy of the whole pantograph at full-band frequencies, SAS ranks the first, followed by IDDES sst-kω, DDES sst-kω, and DDES R-kε.

4.4. Brief Summary. This section evaluates the adaptabilities of the five models in simulating the aeroacoustics of pantograph based on the flow field structure, aeroacoustic source, and radiated noise. It is noteworthy that LES is

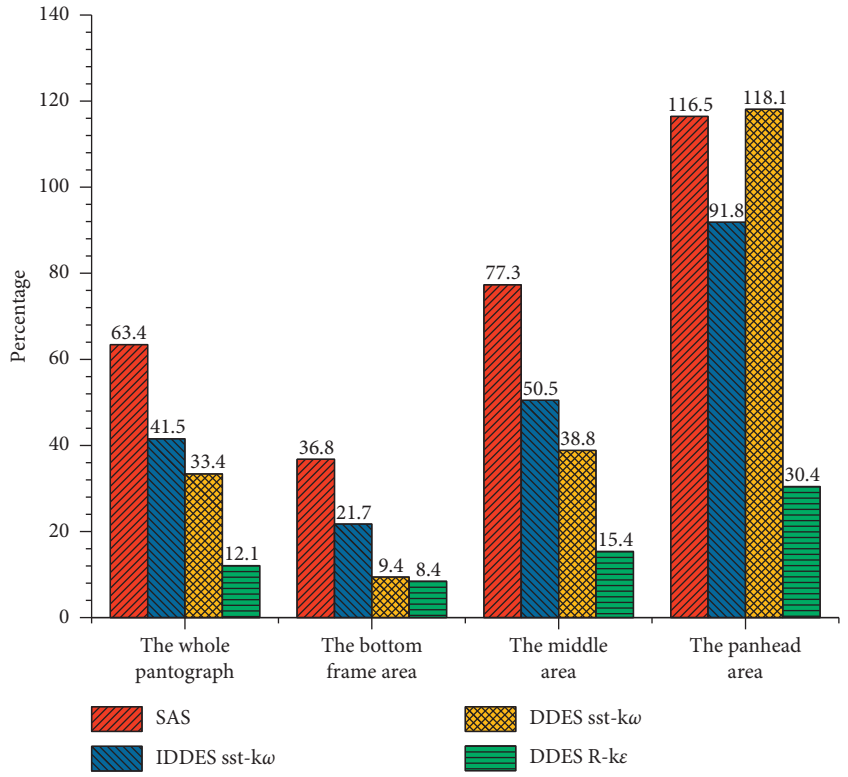

Figure 17: Percentage of equivalent radiated acoustic energy density of the four models at the standard observation point relative to LES (350 km/h).

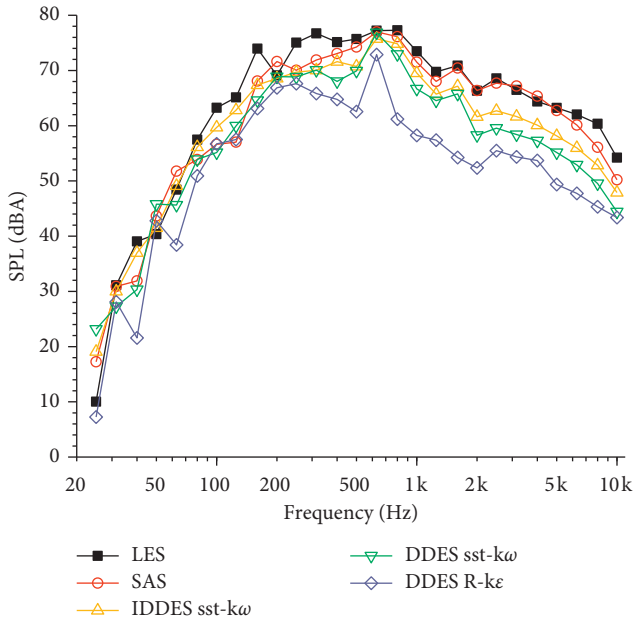

Figure 18: Aeroacoustic frequency spectrum curves of the whole pantograph at the standard observation point.

supposed to be accurate in the light of its refinement in simulating flow field structure and through validation of its numerical simulation results under the condition of limited tests data. By referring to the result from LES, the other four models' performances were investigated. Compared with LES, the results are mostly biased at the underframe regions. Furthermore, the extent of differences that the four models have alters, which in turn leads to discrepancy in simulating aeroacoustic source and radiated noise at underframe region. With regard to the computation precision inflow field structure, aeroacoustic source, and radiated noise, it has an order of SAS, IDDES sst-kω, DDES sst-kω, and DDES R-kε from nice to bad. From engineering precision, SAS, IDDES sst-kω, and DDES sst-kω can replace LES in simulating aeroacoustics of high-speed train pantograph whereas DDES R-kε cannot.

Notably, the five models rank equally in simulating aeroacoustics of cylinder and pantograph; the only difference is that IDDES sst-kω is more suitable than DDES sst-kω for simulating aeroacoustics of pantograph but not for cylinder. This represents higher precision of IDDES sst-kω than DDES sst-kω in simulating aeroacoustics of structures with many rods and plates.

5. Conclusions

In the paper, the performances of LES, SAS, IDDES sst-kω, DDES sst-kω, and DDES R-kε were investigated on simulating flow-field structures, aeroacoustic sources, and aeroacoustics of cylinders and pantographs. As the last part of each section summarizes the detailed conclusions, they are not listed in detail in this section, giving only the ranking of the adaptability of the five turbulence models to the aerodynamic noise of the columns and pantographs.

The computation precision of the five models can be ranked from the best to worst in the following order: LES,

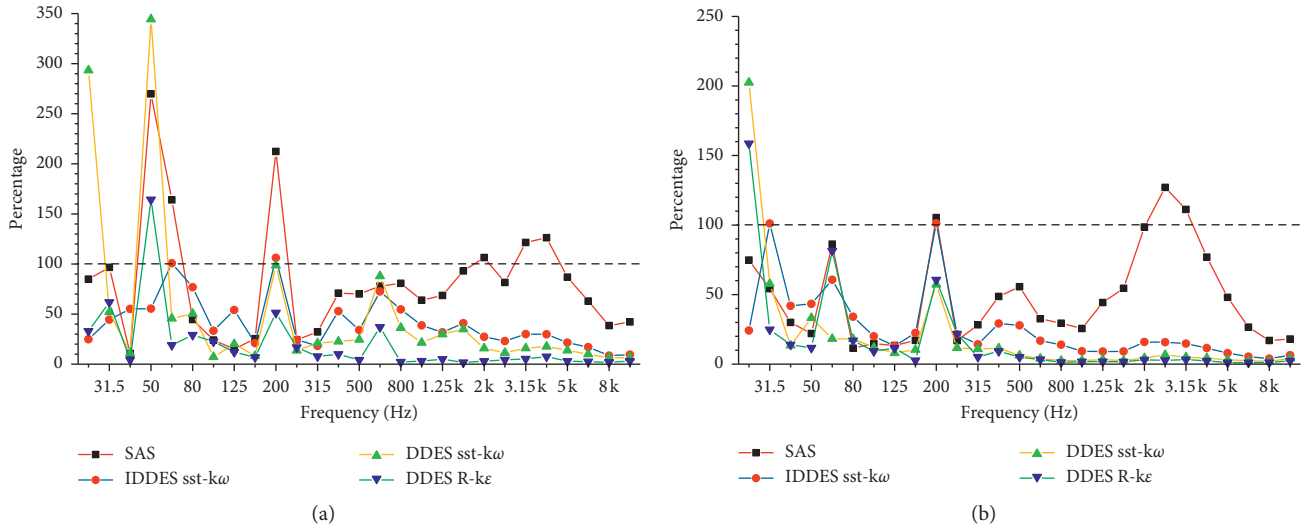

Figure 19: Percentage of equivalent radiated acoustic energy density of the four models relative to LES at all frequencies (350 km/h): (a) whole pantograph; (b) bottom frame area. The dashed line represents the LES result.

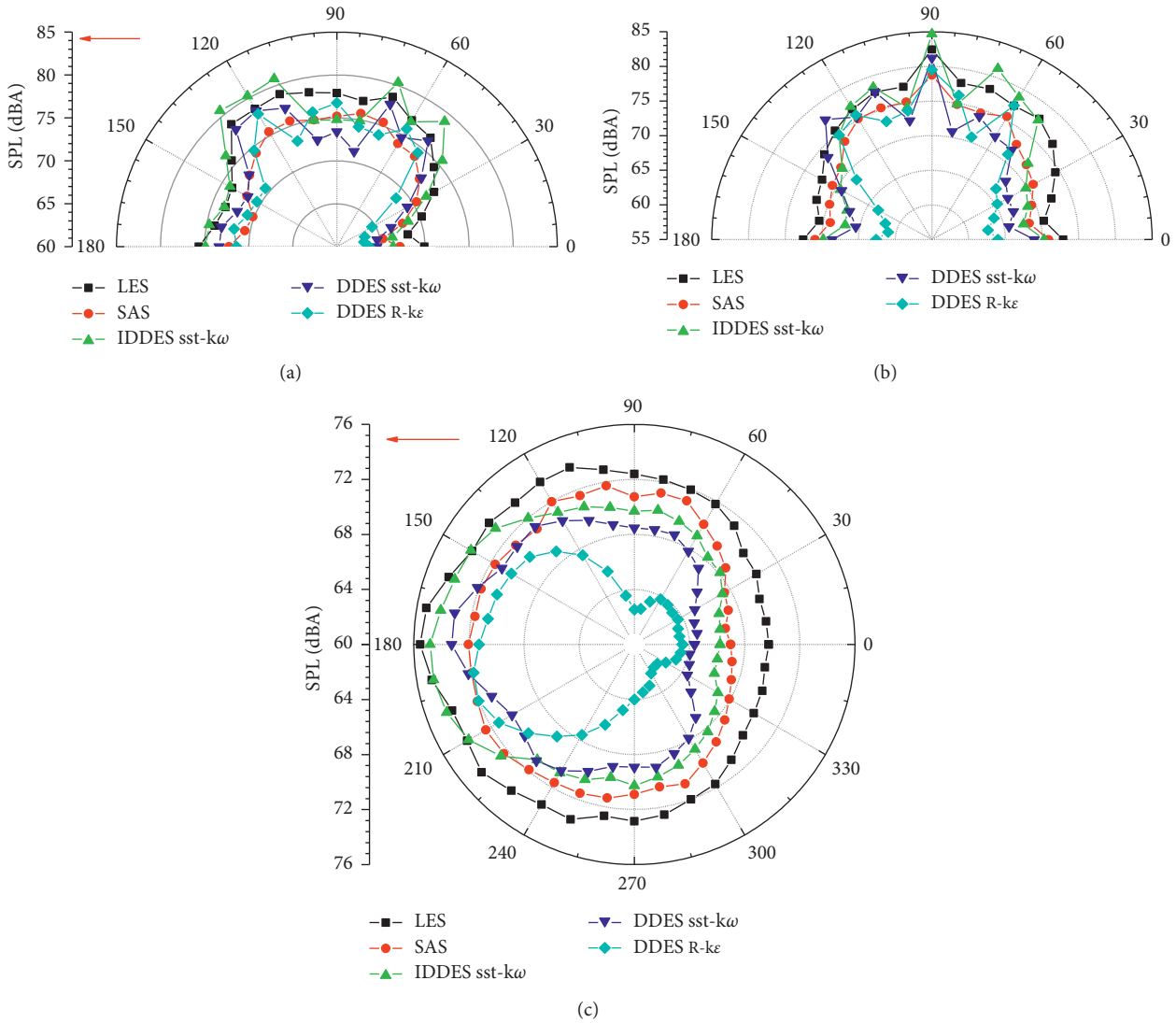

Figure 20: Far-field directionality of radiated noise from pantograph (350 km/h): (a) directionality 1-*xz* plane; (b) directionality 2-*yz* plane; (c) directionality 3-*xy* plane. The arrow in the picture denotes the direction of airflow.

SAS, DDES sst-kω, IDDES sst-kω, and DDES R-kε for cylinder simulation and in the order LES, SAS, IDDES sst-kω, DDES sst-kω, and DDES R-kε for pantograph simulation. Although none of the models can match up to the performance of LES with respect to precision, SAS, DDES sst-kω, and IDDES sst-kω can be used as a substitution of LES in simulating the aeroacoustics of high-speed train pantograph, considering engineering precision.

Data Availability

The computational grid in this paper has several G bytes, which are difficult to put on the disk. The readers can contact the author if they need it (sound_wdq@csu.edu.cn). Other research data in this paper exist in Baidu Disk. The address of the disk is https://pan.baidu.com/s/1OZLHwXYpQ3IsXdVSDXCCnQ. The method of data acquisition is to open the file with office word software in the computer with Origin Software installed and then double-click the corresponding curve graph to obtain the data of the graph.

Conflicts of Interest

The authors declare that there are no conflicts of interest regarding the publication of this paper.

Acknowledgments

This work was supported by Ministry of Education, School of Traffic and Transportation Engineering (2016YFB1200503-03). The authors would like to thank Editage (http://www.editage.cn) for English language editing.

References

[1] J. Zhang, X. Xiao, X. Sheng, C. Zhang, R. Wang, and X. Jin, "SEA and contribution analysis for interior noise of a high speed train," *Applied Acoustics*, vol. 112, pp. 158–170, 2016.

[2] X. Zheng, Z. Hao, X. Wang, and J. Mao, "A full-spectrum analysis of high-speed train interior noise under multi-physical-field coupling excitations," *Mechanical Systems and Signal Processing*, vol. 75, pp. 525–543, 2016.

[3] A. Mao, K. Ehrenfried, S. Loose, and C. Wagner, "Microphone array wind tunnel measurements of Reynolds number effects in high-speed train aeroacoustics," *International Journal of Aeroacoustics*, vol. 11, no. 3-4, pp. 411–446, 2015.

[4] T. Kurita, M. Hara, H. Yamada, F. Wakabayashi, H. Satoh, and T. Shikama, "Reduction of pantograph noise of high-speed trains," *Journal of Mechanical Systems for Transportation and Logistics*, vol. 3, no. 1, pp. 63–74, 2010.

[5] X. M. Tan, Z. G. Yang, X. L. Wu et al., "Experimental research on frequency spectrum component model of noise source outside the CIT500 train," *Journal of the China Railway Society*, vol. 7, pp. 32–37, 2017, in Chinese.

[6] Y. Gao, X. Li, and J. Wu, "Aerodynamic noise research on high-speed train pantograph," *Railway Locomotive & Car*, vol. 37, no. 5, pp. 54–58, 2017, in Chinese.

[7] T. Mitsumoji, T. Sueki, N. Yamazaki et al., "Aerodynamic noise reduction of a pantograph panhead by applying a flow control method," in *Noise and Vibration Mitigation for Rail Transportation Systems*, Springer, Berlin, Heidelberg, Germany, 2015.

[8] C. Noger, J. C. Patrat, J. Peube, and J. L. Peube, "Aero-acoustical study of the TGV pantograph recess," *Journal of Sound and Vibration*, vol. 231, no. 3, pp. 563–575, 2000.

[9] T. Takaishi, M. Ikeda, and C. Kato, "Method of evaluating dipole sound source in a finite computational domain," *Journal of the Acoustical Society of America*, vol. 116, no. 3, pp. 1427–1435, 2004.

[10] M. Ikeda and T. Mitsumoji, "Evaluation method of low-frequency aeroacoustic noise source structure generated by Shinkansen pantograph," *Quarterly Report of RTRI*, vol. 49, no. 3, pp. 184–190, 2008.

[11] M. Ikeda and T. Mitsumoji, "Numerical estimation of aerodynamic interference between panhead and articulated frame," *Quarterly Report of RTRI*, vol. 50, no. 4, pp. 227–232, 2009.

[12] M. Ikeda and T. Mitsumoji, *Evaluation of Aeroacoustic Noise Source Structure around Panhead of a Pantograph in High-Speed Railway*, http://www.uic.org/cdrom/2008/11_wcrr2008/pdf/S.2.4.4.2.pdf.

[13] X. Sun and X. Han, "Numerical modeling and investigation on aerodynamic noise characteristics of pantographs in high-speed trains," *Complexity*, vol. 2018, Article ID 6932596, 12 pages, 2018.

[14] Y. Zhang, J. Zhang, T. Li, and L. Zhang, "Investigation of the aeroacoustic behavior and aerodynamic noise of a high-speed train pantograph," *Science China Technological Sciences*, vol. 60, no. 4, pp. 561–575, 2017.

[15] J.-H. Zhang, S. Jeong, and K. Kim, "Optimal shape of blunt device for high speed vehicle," *International Journal of Aeronautical and Space Sciences*, vol. 17, no. 3, pp. 285–295, 2016.

[16] B. S. Holmes, J. B. Dias, B. A. Jaroux, T. Sassa, and Y. Ban, "Predicting the wind noise from the pantograph cover of a train," *International Journal for Numerical Methods in Fluids*, vol. 24, no. 12, pp. 1307–1319, 1997.

[17] S. A. Lee, H. M. Kang, Y. B. Lee, C. W. Kim, and K. H. Kim, "The aero-acoustic analysis for each part of double arm pantograph of high speed train," *Journal of Computational Fluids Engineering*, vol. 20, no. 2, pp. 61–66, 2015.

[18] X. Liu, "Aerodynamic noise from a train pantograph," in *Proceedings of the 21st International Congress on Sound and Vibration*, Beijing, China, July 2014.

[19] Y. Zhang, J. Zhang, T. Li, L. Zhang, and W. Zhang, "Research on aerodynamic noise reduction for high-speed trains," *Shock and Vibration*, vol. 2016, no. 3, Article ID 6031893, 21 pages, 2016.

[20] H. Kim, "Unsteady aerodynamics of high speed train pantograph cavity flow control for noise reduction," in *Proceedings of the AIAA/CEAS Aeroacoustics Conference*, Lyon, France, May 2016.

[21] S. Lei, "Numerical analysis of aerodynamic noise of a high-speed pantograph," in *Proceedings of the 2013 Fourth International Conference on Digital Manufacturing and Automation (ICDMA)*, Qindao, China, June 2013.

[22] D. Siano, "Numerical modeling and experimental evaluation of an high-speed train pantograph aerodynamic noise," in *Proceedings of the Meeting on Computers and Mathematics in Automation and Materials Science*, Shanghai, China, January 2014.

[23] R. S. Rogallo and P. Moin, "Numerical simulation of turbulent flows," *Annual Review of Fluid Mechanics*, vol. 16, no. 1, pp. 99–137, 1984.

[24] F. R. Menter and M. Kuntz, *A Zonal SST-DES Formulation*, DES Workshop, St Petersburg, Russia, 2003.

[25] P. R. Spalart, S. Deck, M. L. Shur, K. D. Squires, M. K. Strelets, and A. Travin, "A new version of detached-eddy simulation, resistant to ambiguous grid densities," *Theoretical and Computational Fluid Dynamics*, vol. 20, no. 3, pp. 181–195, 2006.

[26] M. L. Shur, P. R. Spalart, M. K. Strelets, and A. K. Travin, "A hybrid RANS-LES approach with delayed-DES and wall-modelled LES capabilities," *International Journal of Heat and Fluid Flow*, vol. 29, no. 6, pp. 1638–1649, 2008.

[27] K. R. Reddy, J. A. Ryon, and P. A. Durbin, "A DDES model with a Smagorinsky-type eddy viscosity formulation and log-layer mismatch correction," *International Journal of Heat and Fluid Flow*, vol. 50, pp. 103–113, 2014.

[28] M. S. Gritskevich, A. V. Garbaruk, J. Schütze, and F. R. Menter, "Development of DDES and IDDES formulations for the k-ω shear stress transport model," *Flow, Turbulence and Combustion*, vol. 88, no. 3, pp. 431–449, 2012.

[29] U. Garbaruk, "Advanced DES methods and their application to aeroacoustics," in *Progress in Hybrid RANS-LES Modelling*, Springer, Berlin, Heidelberg, Germany, 2010.

[30] F. Menter, M. Kuntz, and R. Bender, "A scale-adaptive simulation model for turbulent flow predictions," in *Proceedings of the 41st Aerospace Sciences Meeting and Exhibit*, Reno, NV, USA, January 2003.

[31] J. D. Revell, R. A. Prydz, and A. P. Hays, "Experimental study of aerodynamic noise vs drag relationships for circular cylinders," *AIAA Journal*, vol. 16, no. 6, pp. 889–897, 1971.

[32] H. Q. Zhang, M. Chen, and G. C. Sun, "Comparative study on the flow field and acoustic field simulation for noise prediction induced by the flow around a cylinder," *Noise & Vibration Control*, vol. 36, no. 3, pp. 26–31, 2016, in Chinese.

[33] X.-M. Tan, Z.-G. Yang, X.-M. Tan, X.-L. Wu, and J. Zhang, "Vortex structures and aeroacoustic performance of the flow field of the pantograph," *Journal of Sound & Vibration*, vol. 432, pp. 17–32, 2018.